THE JOURNAL OF BIOLOGICAL CHEMISTRY VOL. 289, NO. 51, pp. 35605–35619, December 19, 2014

Allosteric Inhibition of the Neuropeptidase Neurolysin*

Received for publication, October 22, 2014 Published, JBC Papers in Press, November 5, 2014, DOI 10.1074/jbc.M114.620930

Christina S. Hines[‡1], Kallol Ray[‡2], Jack J. Schmidt[‡], Fei Xiong[‡], Rolf W. Feenstra[§], Mia Pras-Raves[§], Jan Peter de Moes[§], Jos H. M. Lange[§], Manana Melikishvili[‡], Michael G. Fried[‡], Paul Mortenson[¶], Michael Charlton[¶], Yogendra Patel[¶], Stephen M. Courtney[¶], Chris G. Kruse[§], and David W. Rodgers[‡3]

From the [‡]Department of Molecular and Cellular Biochemistry and the Center for Structural Biology, University of Kentucky, Lexington, Kentucky 40536, [§]Abbott Healthcare Products B.V., C.J. van Houtenlaan 36, 1381 CP, Weesp, The Netherlands, and [¶]Evotec (UK) Ltd., 114 Milton Park, Abingdon, OX14 4SA Oxfordshire, United Kingdom

Background: Neuropeptidases metabolize regulatory peptides and hormones.
Results: A new type of neuropeptidase inhibitor binds away from the catalytic site, is noncompetitive with short peptide substrates, and promotes the open enzyme conformation.
Conclusion: The inhibitor restricts a conformational change associated with substrate cleavage.
Significance: Inhibitors of this class will allow more specific modulation of neuropeptidases, aiding therapeutic development.

Neuropeptidases specialize in the hydrolysis of the small bioactive peptides that play a variety of signaling roles in the nervous and endocrine systems. One neuropeptidase, neurolysin, helps control the levels of the dopaminergic circuit modulator neurotensin and is a member of a fold group that includes the antihypertensive target angiotensin converting enzyme. We report the discovery of a potent inhibitor that, unexpectedly, binds away from the enzyme catalytic site. The location of the bound inhibitor suggests it disrupts activity by preventing a hinge-like motion associated with substrate binding and catalysis. In support of this model, the inhibition kinetics are mixed, with both noncompetitive and competitive components, and fluorescence polarization shows directly that the inhibitor reverses a substrate-associated conformational change. This new type of inhibition may have widespread utility in targeting neuropeptidases.

Zinc metallopeptidases are one of the largest classes of enzymes that hydrolyze peptide bonds, with members widely distributed throughout all the kingdoms of life (1). They play vital roles in both development and maintenance of the mature organism and are of considerable interest as therapeutic targets for a range of human disorders. Recently, there have been extensive efforts to develop inhibitors of matrix metalloproteases, which degrade collagen and other components of connective tissue, because of their role in tumor cell invasion and metastasis as well as inflammatory processes associated with arthritis and cardiovascular disease (2, 3). One of the most prominent examples of targeting a metallopeptidase is the use of angiotensin converting enzyme (ACE)[4] inhibitors to treat hypertension (4).

A key function of ACE and other members of the specialized group of metallopeptidases termed neuropeptidases is to regulate and metabolize the hundreds of known bioactive peptides that act as signaling molecules in the central nervous system and periphery (5). These enzymes are restricted to oligopeptide substrates, and they can be either exo- or endopeptidases. The group includes neurolysin (E.C. 3.4.24.16), a 78-kDa enzyme widely distributed in mammalian tissues and found in various subcellular compartments depending on cell type (6). Neurolysin, and the closely related (60% sequence identity) thimet oligopeptidase (TOP), hydrolyze many bioactive peptides *in vitro* (7, 8), exemplifying the ability of some neuropeptidases to target diverse cleavage site sequences. Their most established role *in vivo* is in the metabolism of neurotensin, a bioactive tridecapeptide, which is cleaved by neurolysin between its 10th (Pro) and 11th (Tyr) residues to produce inactive or largely inactive fragments. Neurotensin is involved in an array of processes including mast cell degranulation (9) and regulation of central nervous system dopaminergic and cholinergic circuits (10, 11). A decrease in neurotensin levels is associated with schizophrenia (12), and antipsychotic drugs increase the level of neurotensin in the midbrain, possibly one of the mechanisms mediating their physiological effects (13). In addition, neurotensin is implicated in cardiovascular disorders (14, 15) and addiction (16), as well as Huntington and Parkinson diseases (10), and it is one of the most potent blockers of pain perception (17).

Neurolysin has an overall prolate ellipsoid shape, with a deep narrow channel dividing it into two roughly equal domains (I and II) (18). The catalytic site, which is contained within a thermolysin-like (19) region found in many metallopeptidases, is located in domain I near the floor of the channel, where it is accessible to only short, unstructured, oligopeptide substrates. TOP has an essentially identical fold (20), as does another M3 family member, dipeptidyl carboxypeptidase (21). Unexpect-

* This work was supported, in whole or in part, by National Institutes of Health Grant NS38041 (to D. W. R.).
The atomic coordinates and structure factors (code 4FXY) have been deposited in the Protein Data Bank (http://wwpdb.org/).
[1] Fellow of the National Institute on Drug Abuse supported by Grant DA14596.
[2] Fellow of the American Heart Association Ohio Valley Affiliate.
[3] To whom correspondence should be addressed: 741 South Limestone, Lexington, KY 40536-0509. Tel.: 859-257-5205; Fax: 859-257-2203; E-mail: david.rodgers@uky.edu.

[4] The abbreviations used are: ACE, angiotensin converting enzyme; TOP, thimet oligopeptidase; Boc, *t*-butoxycarbonyl.

edly, the fold architecture of neurolysin and TOP has been found in members of other metallopeptidase families, notably ACE (22), ACE-related carboxypeptidase (ACE2) (23), and *Pyrococcus furiosus* carboxypeptidase (24). This fold therefore appears to be a widespread adaptation of the thermolysin domain that restricts these enzymes to short oligopeptide substrates.

Comparison of the known crystal structures of enzymes with the neurolysin/TOP-fold suggests that a substantial conformational change is stabilized by substrate or substrate-analog binding (21, 23). Unliganded ACE2 has a conformation similar to that of neurolysin, with a channel of approximately the same width (23). Binding of a substrate-like inhibitor at the catalytic site, however, was seen to be associated with a hinge-like motion that rotates the two domains toward each other, closing the channel around the ligand. In addition, the crystal structures of dipeptidyl carboxypeptidase (21) and ACE (22, 25) with ligands bound at their active sites are also in closed conformations. Thermolysin itself (26) and other enzymes with thermolysin-like catalytic domains, such as astacin (27), undergo hinge-like motions upon ligand binding. A conformational change associated with the catalytic cycle thus may be inherent to this group of metallopeptidases.

Inhibition of neuropeptidases is an effective approach for modulating the levels of their neuropeptide substrates or products, as demonstrated by the ACE inhibitors (4). An inhibitor of neurolysin has been shown to produce neurotensin-induced analgesia in mice (28), and the control of neurotensin levels by neurolysin (along with TOP) makes it an attractive target for antipsychotic therapies. Several relatively selective inhibitors of neurolysin and TOP, such as phosphodiepryl 08, have been developed (29–31). These compounds, like nearly all known metallopeptidase inhibitors, bind at the catalytic site and coordinate the zinc ion cofactor. As such, they carry phosphinic or carboxylic acid moieties that result in little or no brain penetration with oral administration. Conversion of these types of inhibitors into effective therapeutics has been problematic, and new classes of compounds are needed to expand the targeting of neuropeptidases and metallopeptidases in general. We report here the characterization of an inhibitor of neurolysin that binds remotely from the catalytic site and reduces enzyme activity by an allosteric mechanism. This and related compounds represent a promising new class of inhibitors that should prove useful with other members of this zinc metallopeptidase group.

EXPERIMENTAL PROCEDURES

Syntheses of Compounds R1 and R2

^{1}H and ^{13}C NMR spectra were recorded on 600 or 300 MHz instruments using $CDCl_3$ as solvent with tetramethylsilane as an internal standard. Chemical shifts are given in parts per million (ppm) (d scale) downfield from tetramethylsilane. Coupling constants (*J*) are expressed in hertz (Hz). Flash chromatography was performed using Silica Gel 60 (0.040–0.063 mm, Merck). Mass spectra were recorded on a Micromass QTOF-2 instrument with MassLynx application software for acquisition and reconstruction of the data. Exact mass measurement by HRMS was done of the quasimolecular ion $[M + H]^+$.

*1,5-Bis-(2-chloro-phenyl)-pyrazolidine (**R5**) (Fig. 1A)*—Under a nitrogen atmosphere, 2-chlorophenylhydrazine hydrochloride (**R4**) (20.0 g, 111.7 mmol) was added to a mixture of water (5.0 ml) and acetic acid (60 ml) at 0 °C. Then 12.3 ml of concentrated sulfuric acid was added. 2-Chlorostyrene (**R3**) (15.4 g, 111.4 mmol) and paraformaldehyde (3.4 g, 113 mmol) were added to the mixture portionwise. After 1 h at 0 °C the mixture was left overnight with stirring at ambient temperature. Then the reaction mixture was poured onto water (~200 ml) at 0 °C, and the whole mixture was extracted with Et_2O (2 × 100 ml). Layers were separated and the water layer was brought to pH > 10 (50% NaOH) and extracted with CH_2Cl_2 (3 × 100 ml). The combined organic fractions were dried on $MgSO_4$. Removal of the drying agent by filtration and concentration *in vacuo* of the filtrate yielded 25 g of a yellow oil containing **R5**. This was used in the next step without further purification as **R5** is unstable.

*{2-[2,3-Bis-(2-chloro-phenyl)-pyrazolidin-1-yl]-2-oxo-ethyl}-carbamic acid tert-butyl ester (**R7**)*—Pyrazolidine (**R5**) (5.0 g, 17.1 mmol) and Boc-glycine (**R6**) (3.0 g, 17.1 mmol) were dissolved in acetonitrile (65 ml). Dicyclohexyl carbodiimide (4.6 g, 22.2 mmol, 1.3 eq) was added. After stirring overnight the suspension was filtered and the residue was washed with acetonitrile. The combined organic fractions were concentrated *in vacuo* and the residue was subjected to flash column chromatography (SiO_2, eluent: CH_2Cl_2, then CH_2Cl_2/MeOH, 9:1). CH_2Cl_2 elution gave apolar fractions containing byproducts, during CH_2Cl_2/MeOH, 9:1, elution pure fractions containing **R7** were obtained. After concentration *in vacuo*, 6.0 g of **R7** was isolated as a glass.

*2-Amino-1-[2,3-bis-(2-chloro-phenyl)-pyrazolidin-1-yl]-ethanone (**R8**)*—The Boc protected **R7** (6.0 g, 13.3 mmol) was dissolved in dry CH_3CN (35 ml) under a nitrogen atmosphere. Then Me_3SiCl (2.53 ml, 20 mmol, 1.5 eq) was added followed by KI (3.3 g, 20 mmol, 1.5 eq). The mixture was stirred for 16 h after which 200 ml of 5% $NaHCO_3/H_2O$ and 350 ml of EtOAc were added. Vigorous stirring was continued for 1.5 h. Solid material was removed by filtration, and the organic layer dried on $MgSO_4$. Removal of the drying agent by filtration and concentration *in vacuo* of the filtrate yielded 4.6 g of the desired product **R8**. This was used in the next step without further purification.

*1-Adamantan-2-yl-3-{2-[2,3-bis-(2-chloro-phenyl)-pyrazolidin-1-yl]-2-oxo-ethyl}-urea (**R1**)*—4.6 g (13.1 mmol) of **R8** was dissolved with slight heating in CH_3CN (65 ml). At room temperature, a suspension of isocyanate **R9** (2.33 g, 13.1 mmol, 1 eq) in CH_3CN (20 ml) was added to the reaction mixture. The mixture was stirred overnight and filtered to yield 4.3 g of a white solid that was subjected to column chromatography (SiO_2, eluent: EtOAc). This gave 2.7 g of a white solid that was recrystallized from CH_3CN (175 ml), yielding 1.9 g of pure **R1** melting point 163–6 °C.

*5-(2-Chlorophenyl)-1-(2-fluorophenyl)pyrazolidine (**R11**) (Fig. 1B)*—2-Fluorophenylhydrazine hydrochloride **R10** (25 g, 153.8 mmol) was added to a mixture of water (3.8 ml), acetic acid (31 ml), and sulfuric acid (12.5 ml) at 0 °C. 2-Chlorostyrene (**R3**)

(21.3 g, 153.8 mmol) and 90% paraformaldehyde (5.1 g, 153.8 mmol) were added to the mixture. After 1 h at 0 °C the mixture was left overnight with stirring at ambient temperature. The resulting dark brown solution was diluted with water (100 ml), while maintaining the temperature below 5 °C with an ice-water bath. Non-acid soluble side products were extracted with diethyl ether (150 ml). The aqueous layer was made alkaline with sodium hydroxide solution (33%, 100 ml) and the liberated pyrazolidine (**R11**) was extracted with TBME (1 × 200 ml, 2 × 100 ml). Combined extracts were washed with water (50 ml) and brine (50 ml). After drying with sodium sulfate the solvent was evaporated to leave a brownish oil (38.9 g, 85%). HPLC-MS: $(M^{35}Cl + H)^+$ 277.1, $(M^{37}Cl + H)^+$ 279.2, ^1H NMR ($CDCl_3$, 300 MHz, δ ppm): 1.8–2.0 (1H, m), 2.9–3.0 (1H, m), 3.0–3.1 (1H, m), 3.2–3.4 (2H, m), 5.0 (1H, d), 6.8–7.7 (8H, m). The oil was used in the next step without purification. Storage at −20 °C under a nitrogen atmosphere was used to slow down the oxidation of the pyrazolidine nucleus.

*tert-Butyl-N-[1-[3-(2-chlorophenyl)-2-(2-fluorophenyl)pyrazolidin-1-yl]-1-oxopropan-2-yl]carbamate (R) (**R13**)*—Pyrazolidine (**R11**) (4.44 g, 16.1 mmol) and Boc-L-alanine (**R12**, 3.05 g, 16.1 mmol) were dissolved in acetonitrile (50 ml). Dicyclohexyl carbodiimide (4.2 g, 20.4 mmol) was added. A colorless solid (dicyclohexylurea) was immediately precipitated. After stirring overnight the suspension was filtered and the residue was washed with acetonitrile. The combined filtrates were concentrated *in vacuo* to yield 8.87 g of a sticky amber mass. Solvent gradient chromatography (ethyl acetate/heptane, 1:4) yielded two fractions (fraction 1: 2.7 g (S)-**R13**, fraction 2: 1.4 g (R)-**R13**). HPLC-MS: $(M^{35}Cl + H)^+$ 448.2, $(M^{37}Cl + H)^+$ 450.2. The latter fraction ((R)-**R13**) was used in the next step.

*2-Amino-1-[3-(2-chlorophenyl)-2-(2-fluorophenyl)-1-pyrazolidinyl]-1-propanone (R) (**R14**)*—1.25 g (3.6 mmol) of Boc-amine (R)-**R13** was dissolved in trifluoroacetic acid/dichloromethane/water (70:25:5, v/v/v) and stirred for 2.5 h. Evaporation of the solvents yielded the crude amine (R)-**R14** (0.69 g, 37%). HPLC-MS: $(M^{35}Cl + H)^+$ 348.2, $(M^{37}Cl + H)^+$ 350.3. ^1H NMR ($CDCl_3$, 300 MHz, δ ppm): 1.3 (3H, d), 1.7 (s(br), 2H), 2.2–2.3 (1H, m), 2.7–2.8 (1H, m), 3.7–3.9 (1H, m), 3.9–4.3 (2H, m), 5.0 (1H, d), 6.9–7.5 (8H, m).

*3-[(2S)-1-[(3R)-3-(2-Chlorophenyl)-2-(2-fluorophenyl)pyrazolidin-1-yl]-1-oxopropan-2-yl]-1-(adamantan-2-yl)urea (**R2**)*—0.65 g (1.86 mmol) of (R)-**R14** was suspended in acetonitrile (15 ml). 2-Adamantane isocyanate (**R9**) (0.33 g, 1.86 mmol) was added in one portion to the suspension and stirring was continued for 4 h. The reaction mixture was evaporated to dryness and the residue was purified via solvent gradient chromatography yielding a colorless product containing **R2** (0.61 g, 62%). HPLC-MS: $(M^{35}Cl + H)^+$ 525.2, $(M^{37}Cl + H)^+$ 527.3. ^1H NMR ($CDCl_3$/dimethyl sulfoxide-d_6 1:5 (v/v), 600 MHz, δ ppm): 1.34 (d, J = 6 Hz, 3H), 1.4–1.9 (m, 14H), 2.20 + 2.62(2m, 2H), 3.61 (m, 1H), 4.02(m, 2H), 4.53 (m, 1H), 4.90 (m, 1H), 7.02 (2m, 1H), 7.10 (t, J = 7.5 Hz, 1H), 7.16 (m, 1H), 7.19 (t, J = 7.5 Hz, 1H), 7.29 (t, J = 7.5, 1H), 7.44 (d, J = 7.5 Hz, 1H), 7.53 (d, J = 7.5 Hz, 1H). ^{13}C NMR($CDCl_3$/dimethyl sulfoxide-d_6, 1:5, 150 MHz, δ ppm): 19.3, 27.5, 27.6, 32.0(3), 33.0(2), 37.7(2), 38.1, 45.5, 47.5, 53.7, 67.2, 117.1 (J_{CF} = 21 Hz), 118.4, 124.4 (J_{CF} = 8 Hz), 125.3 Hz, 127.8, 128.3, 129.5, 129.9, 131.5, 138.7 (J_{CF} = 8 Hz), 139.7, 153.3 (J_{CF} = 244 Hz), 157.6, 171.0. HRMS ($C_{29}H_{35}N_4O_2{}^{35}ClF$) $[M + H]^+$: found m/z 525.2447, calculated 525.2433. Note: the amide bond gives rise to two rotamers, and the ^1H NMR data belong to the most abundant rotamer. Both NMR experiments were conducted at 10 °C.

Neurolysin Expression Constructs

The rat neurolysin used is a point variant of the construct employed in previous studies (18, 32). In this variant, which was expressed in *Escherichia coli* using a pBAD/His vector (Invitrogen), a surface histidine (His-160) involved in a divalent cation-mediated lattice contact in the original neurolysin crystals was converted to an alanine during attempts to obtain new crystal forms. The H160A mutation, as well as the E475A mutation of the catalytic glutamate residue, were introduced using the QuikChange kit (Stratagene). Primers for generating neurolysin mutant constructs were obtained from Operon Biotechnologies, Inc. and diluted with distilled water to 100 ng/ml. Reactions consisted of 5 ml of 3.5 ng/ml of template, 1.25 ml of each primer at 100 ng/ml, 1.0 ml of 20 mM dNTP mixture, 5 ml of 10× *Pfu* Reaction Buffer, 35.5 ml of distilled water, and 1 ml of *Pfu* DNA polymerase at 2.5 units/ml. Methylated template DNA was then digested by adding 1 ml of DpnI to the reaction tube and incubating at 37 °C for 2 h. The product was run at the expected linearized size of 6.1 kb on an agarose gel. PCR DNA was ligated overnight at room temperature (5 ml of DNA, 1 ml of reaction buffer, 3 ml of distilled water, and 1 ml of T4 DNA ligase) then transformed into TOP10 *E. coli* competent cells (Invitrogen). The pBAD/His neurolysin H160A and E475A constructs were sequenced (University of California Davis DNA Sequencing Facility) to confirm the desired mutations and the absence of any unwanted substitutions.

Protein Expression, Purification, and Cocrystallization

Protein expression and purification were performed as described previously (18, 32). Initial crystallization conditions were determined using commercial screens (Hampton). Optimized crystals were produced by hanging drop vapor diffusion, mixing 2 ml of 48 mM protein in the presence of 5-fold stoichiometric excess of inhibitor **R2** with 1 ml of well solution containing 0.1 M HEPES, pH 7.0, 0.1 M $LiSO_4$, 2 mM 2-mercaptoethanol, and 12–15% polyethylene glycol 4000. The stock solution of **R2** was 5 mM in dimethyl sulfoxide. Crystals were grown at 4 °C and formed as individual, rhombohedral plates with dimensions ~100 mm × 200 mm × 10 mm.

Data Collection and Structure Determination

Crystals were flash cooled in liquid nitrogen after soaking for about 5 s in a solution having the same composition as the well solution plus 20% polyethylene glycol 400. Data were collected at −160 °C at the Structural Biology Center (SBC) beamline 19-ID and the Southeast Regional Collaborative Access Team (SER-CAT) beamline 22-ID of the Advanced Photon Source, Argonne National Laboratory, and reduced using HKL2000 (33). Data were integrated to 2.8 Å with an overall R_{sym} of 14.7% (Table 1). The two molecules of neurolysin in the asymmetric unit were built and refined independently using CNS (34) and PHENIX (35) to an overall R_{work}/R_{free} of 0.235/0.287. Refine-

TABLE 1
Crystallographic data and refinement statistics

	Neurolysin-R2
Data collection	
Space group	$P2_12_12_1$
Cell dimensions	
a, *b*, *c* (Å)	88.0, 131.4, 144.8
α, β, γ (°)	90.0, 90.0, 90.0
Resolution (Å)	20.0–2.8 (2.95–2.80)[a]
R_{merge}	0.162 (0.440)
$I/\sigma I$	8.8 (3.14)
Completeness (%)	99.7 (99.7)
Redundancy	4.1 (4.1)
Refinement	
Resolution (Å)	48.7–2.8
No. reflections	41,891
Completeness (%)	99.6
R_{work}/R_{free}	0.235/0.287
No. molecules in a.u.	2
No. atoms	
Protein	10,670
Ligand/ion	76
Water	257
	127 for protein chain P
	130 for protein chain Q
B-factors	
Proteins	29.4
Ligands	22.7
Ions	24.3
Water	21.4
Root mean square deviations	
Bond lengths (Å)	0.005
Bond angles (°)	0.807

[a] Indicates the statistics for the last resolution shell are shown in parentheses.

ment restraints for **R2** were constructed by generating initial files using the HIC-Up utility (36) and then modifying the values manually as required. Rebuilding and analysis were done using the programs O (37) and COOT (38). The final structure includes amino acid residues 15–678, one zinc atom, and one inhibitor **R2** for each of the two neurolysin molecules in the asymmetric unit. For the protein, 99.7% of the residue backbone angles are in the most favored or additionally allowed regions. A total of 257 solvent molecules were placed. Figures depicting the structure were made with RIBBONS (39), GRASP (40), LIGPLOT (41), and PyMol (open source).

Inhibition Kinetics

Inhibition kinetics for compound **R2** were determined using internally quenched fluorogenic peptide substrates having the amino acid sequenced of dynorphin A(1–8) and neurotensin (Peptides International). These peptides have amino-terminal *o*-aminobenzoate and carboxyl-terminal *N*-(2,4-dinitrophenyl)-ethylenediamine fluorescent donor/acceptor pairs. The increase in fluorescence upon cleavage of these substrates was monitored with a PerkinElmer LS-55 Luminescence spectrometer, using an excitation wavelength of 319 nm and monitoring emission at 419 nm, with reading taken every 0.1 s.

Activity was monitored at 37 °C in a reaction buffer of 25 mM HEPES, pH 7.5, 10 mM NaCl, 0.1 mg/ml of BSA, and 1.5 mM CHAPS using a silanized quartz cuvette with a final reaction volume of 150 μl. Nominal substrate concentrations for dynorphin A(1–8) were 0.25, 0.5, 1.0, and 2.0 μM, and for neurotensin they were 0.125, 0.25, 0.5, and 1.0 μM. Inhibitor concentrations for both peptide substrates were 0, 30, 90, and 270 nM. Neurolysin concentration was either 8 or 16 nM for the dynorphin A(1–8) reactions and either 4 or 8 nM for the neurotensin reactions. Kinetic progress curves were recorded until the reaction reached or approached a plateau in fluorescence intensity.

Fit of the progress curves to different kinetic inhibition models was done with the program DynaFit (42, 43), which performs nonlinear least-squares regression analysis of kinetic data using rate equations derived from input models. Rate constants for standard competitive, noncompetitive, uncompetitive, and mixed inhibition models (43, 44) were refined globally against progress curve data for each substrate using the Levenberg-Marquardt algorithm (45). Substrate and inhibitor concentrations were fit locally for each progress curve. Initial estimates were determined using the systematic scanning utility in DynaFit, and asymmetric confidence intervals for model parameters were estimated using the profile-t method (46, 47) as implemented in DynaFit. Fisher's F-statistic for nested models (42, 43, 48) was used to discriminate among the different inhibition models.

Fluorescence Polarization

Purified neurolysin was labeled with pyrene fluorescent groups at accessible cysteine positions using *N*-(1-pyrene)-maleimide (Invitrogen, Molecular Probes) following the protocol supplied by the manufacturer. Pyrene was chosen as the fluorescent probe because its long fluorescent lifetime would provide the best opportunity to assess the relatively slow rotational rates of the large enzyme. The labeling reaction went to completion in 3 h, and the modified protein was then separated from unreacted label by passage over a small G-25 size exclusion column. The labeled enzyme retained 75% of the wild type activity in a kinetic assay with the fluorgenic neurotensin substrate. Fluorescence polarization measurements were made at 395 nm on a LS55 luminescence spectrometer (PerkinElmer Life Sciences) using an excitation wavelength of 345 nm. The neurolysin concentration was 0.75 μM, and, when present, the inhibitor (PPD08 or **R2**) was at a concentration of 2 μM.

The limiting polarization was determined by measuring fluorescence polarization in a series of solutions containing 0, 12.5, 25, and 37.5% polyethylene glycol 8000 at 11, 16, and 20 °C. The composite fluorescence lifetime at 395 nm was measured using a LaserStrobe lifetime spectrofluorometer (Photon Technology International) equipped with a model GL-301 dye laser, and the data were analyzed with FeliX32 software (Photon Technology International). The program HYDROPRO (49) was used to calculate the expected difference in polarization for the open conformation of neurolysin (Protein Data Bank code 1I1I) (18) and a model for the closed form based on the ACE2 crystal structure (Protein Data Bank code 1R4L) (23). The calculated polarization value does not change significantly when the additional mass of bound PPD08 or **R2** was included.

Velocity Sedimentation

The conformation of neurolysin under various conditions was monitored by velocity sedimentation ultracentrifugation at 4 °C using a Beckman Coulter ProteomeLab XL-A analytical ultracentrifuge and a AN 60 Ti rotor spinning at 40,000 rpm. The distribution of protein in the cells was monitored at 4-min

intervals by absorbance at 280 nm with a scan step size of 0.001 cm. Catalytically compromised neurolysin E475A mutant was present at concentrations of 2.2, 1.1, or 0.55 μM in 25 mM Tris, pH 7.5, 2 mM 2-mercaptoethanol, and 100 mM NaCl. Where included, dynorphin A(1–8) (Sigma) was at a concentration of 110 μM, and the inhibitor **R2** was at a concentration of 3 μM. Over the course of the experiments (about 4 h), less than 5% of the peptide will be hydrolyzed in the absence of **R2** by the neurolysin mutant based on separate measurements under the same conditions. Data were analyzed using the program SEDFIT (50), which implements a finite element numerical approach to evaluating the Lamm transport equation (51). Solvent density and viscosity were estimated from tabulated values using the program SEDNTERP (52) (2 mM 2-mercaptoethanol present in all samples was not included in the calculation), and the partial specific volume of the protein was estimated from its amino acid composition by the method of Cohn and Edsall (53). The *s* value distributions were corrected to standard conditions of pure water at 20 °C for presentation.

Substrate Binding Models

Dynorphin A(1–8) and neurotensin were docked into the active site channel of neurolysin using the crystal structure coordinates (Protein Data Bank code 1I1I) of the enzyme (18). Peptide coordinates for the appropriate sequences were generated in COOT (38) and manually placed in the neurolysin active site based on the ligand bound structures of members of the same fold group (21–23, 25). The peptides positions were then refined using the FlexPepDock server (54, 55), which allows flexibility of the peptide and nearby protein side chains. For each peptide, the top few models showed only minor variation in the mode of peptide binding, and the highest scoring model was used.

RESULTS

Discovery of the Pyrazolidine Class of Inhibitors—A high-throughput screening with neurolysin was performed and yielded a hit class containing a pyrazolidine ring (56). Optimization led to the potent inhibitor compound **R1** (Fig. 1*A*), which exhibited a $p\mathrm{IC}_{50}$ value of 6.6 ± 0.1. The compound is comprised of a 10-carbon tricyclic adamantyl group, a peptide-like linker segment, and a five-member pyrazolidine ring linked at the N1 and C5 positions to two halogen substituted benzyl rings. The adamantyl group, the smallest member of the diamonoid family, provides a strongly hydrophobic region to the otherwise relatively polar molecule. Interestingly, the compound does not have standard Zn^{2+} interacting moieties present in other zinc metallopeptidase inhibitors. The purified *R* diastereomer with a fluorine for chlorine substitution and a methyl group added to the linker, compound **R2** (Figs. 1*B* and 2*A*), is a more potent inhibitor ($p\mathrm{IC}_{50}$ value of 7.5 ± 0.14) and was used for the studies presented here.

R2 Binds to Neurolysin Away from Its Catalytic Site—A recombinant mutant (H160A) neurolysin construct containing 681 residues was crystallized in the presence of inhibitor **R2**. The structure was determined by molecular replacement using the coordinates of the unliganded enzyme (18) and refined against data to 2.8 Å. As in the unliganded enzyme, the N-terminal 14 and C-terminal 3 residues were disordered in the crystal structure despite different growth conditions and lattice packing. Other general features of the structure also mirror those of the unliganded enzyme.

A difference electron density map (where calculated structure factor amplitudes were taken from the rigidly placed, but otherwise unrefined, unliganded neurolysin model) initially revealed strong positive electron density for bound inhibitor **R2** (Fig. 2*B*). The inhibitor interacts at a single site unexpectedly located at the far end of the central channel of the enzyme. In this position, the closest atom of the inhibitor is over 19 Å from the catalytic site zinc ion (Fig. 2*C*). Other small metallopeptidase inhibitors with known binding sites interact with the catalytic site region, nearly always targeting the zinc ion itself, to sterically block substrate access (57, 58). The electron density for the inhibitor in the refined structure is clear and unambiguous (Fig. 2*D*).

The inhibitor binding site is a surface pocket located underneath helices 1 and 3 of the enzyme (18). Residues in helices 2 and 4 form two sides of this pocket, and its floor is made up of residues from helix 5, which connects the two domains at one end of the channel, and the extended loop connecting helices 16 and 17. Most of the bound inhibitor is buried in the pocket (Fig. 3*A*), with only O1 and C8 in the linker and most of the atoms in the F ring (C12–16, F1) more than minimally solvent exposed. The adamantyl group inserts into a hydrophobic recess of the pocket lined by residues from helices 1–5 (Fig. 3*B*), and the pyrazolidine ring and the C ring tuck against helix 2 in the back of the pocket.

Computational docking studies support the location of the crystallographically determined binding site. Using the coordinates of unliganded neurolysin (18), possible binding sites were identified with the site-finder algorithm in MOE (Chemical Computing Group), which locates surface pockets with substantial hydrophobic character and nearby polar regions. Subsequent docking studies targeting these sites were carried out with the Gold software package (Cambridge Crystallographic Data Centre), and a high-scoring binding mode in the site located crystallographically was obtained (Fig. 3*C*). Significantly, no high scoring binding was seen in the region of the catalytic site.

Only Small Conformational Changes Accompany Inhibitor Binding—Just minor backbone shifts confined to the binding site occur upon formation of the inhibitor-protein complex (Fig. 4, *A* and *B*). The largest movement occurs in the C terminus of helix 3 just above the bound inhibitor. The last three turns of this helix (residues 104–115) shift an average of 1 Å based on Cα positions, with a maximal displacement of 1.6 Å at Ser-114 adjacent to the linker region of **R2**. Without this shift of helix 3, the backbone and side chain atoms at residue positions 114 and 110 would clash with the inhibitor. There are also small backbone shifts in the turn between helices 1 and 2 as well as at the nearby C terminus of helix 4 and the turn to helix 5. These regions are more distant from the binding site, and the shifts are likely the result of differences in packing contacts in the different crystal forms. Differences in packing contacts also account for the backbone shifts in loops at the other end of the channel.

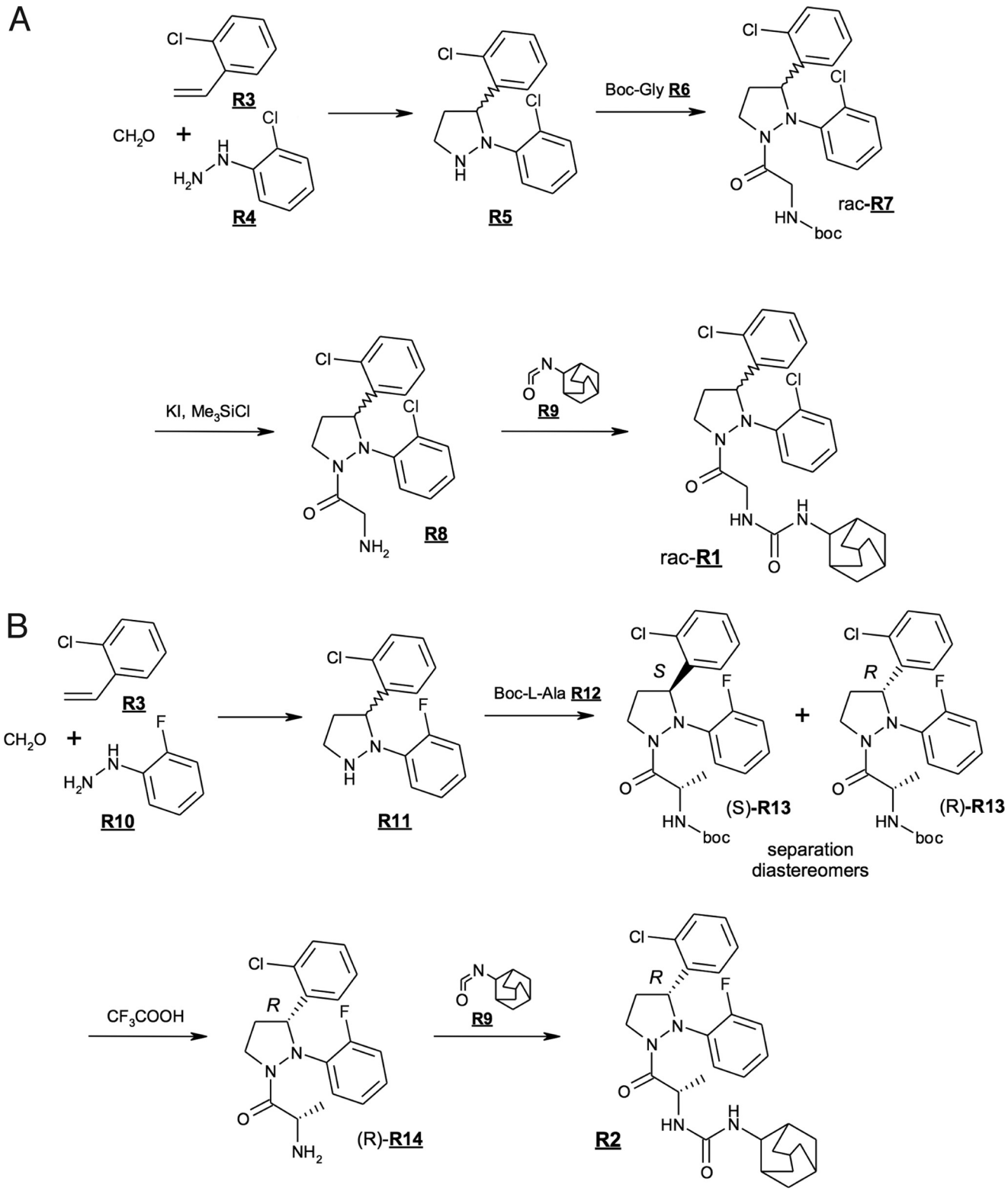

FIGURE 1. **Synthesis of inhibitory compounds R1 and R2.** Major steps in the synthesis of *A*, compound **R1**, and *B*, compound **R2**.

The C terminus of helix 3 moves largely as a rigid unit, with no substantial changes in side chain conformation. A few side chains arising from other secondary elements do alter conformation to accommodate the inhibitor, however. Ile-123 changes side chain rotamer (accompanied by changes at Leu-66 and Leu-143) to make room for the adamantyl group. Met-149 also adopts another rotamer conformation, in this case to bring the side chain into steric contact with the adamantyl. Two remaining changes create space for the C ring. Glu-73 alters side chain conformation, its new position made possible by a coordinated motion of Ile-77 and the side chain of Tyr-49. Overall, only a modest number of conformational changes are

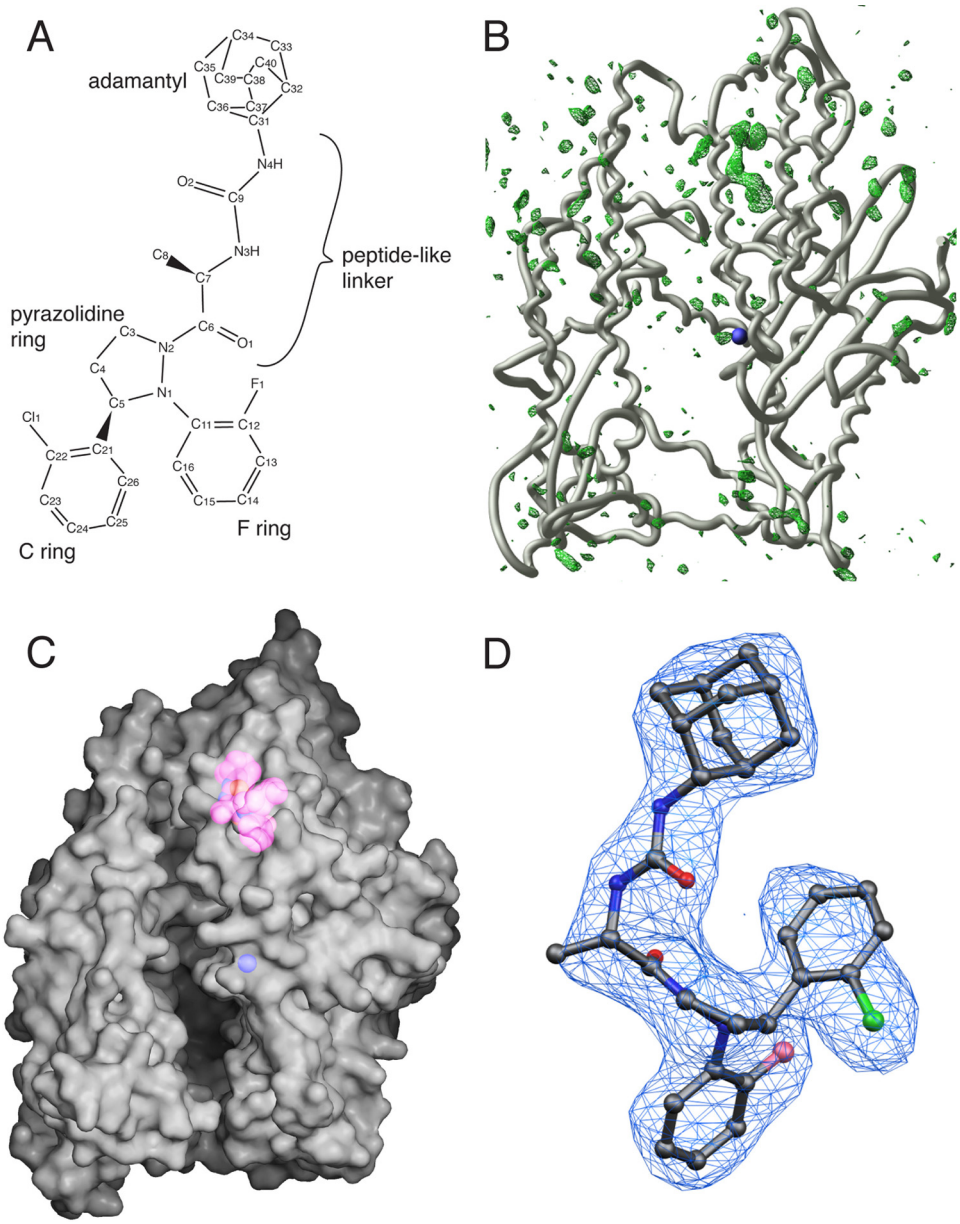

FIGURE 2. **Inhibitor R2 and overview of binding to neurolysin.** *A*, chemical structure of the inhibitor **R2.** *B*, difference ($F_o - F_c$) electron density (*green mesh*) shown at a 3.0 σ contour superimposed on a Cα trace of the final protein model. *C*, semitransparent molecular surface view of neurolysin with the active site channel, bound inhibitor (*magenta*), and catalytic zinc ion (*blue sphere*) visible. *D*, SIGMAA weighted $2F_o - F_c$ electron density for the bound **R2** inhibitor in the fully refined model. The density (*blue mesh*) is displayed at a 0.8 σ contour.

required to accommodate **R2** in the protein, and the largely preformed nature of the site likely contributes to the strength of the interaction.

No structural effects of **R2** binding propagate to the catalytic site region (Fig. 4*C*). Comparing the inhibitor complex and the unliganded enzyme within a 10-Å sphere centered on the catalytic site, the overall root mean square deviation for all nonhydrogen protein atoms is 0.33 Å, which is similar to the coordinate error estimated in refinement (35) of 0.28 Å. Several solvent molecules near the catalytic site present in the unliganded model were not placed in the inhibitor bound enzyme, but this difference probably results from the lower resolution of the data from the complex crystals. Thus, the structural data indicate that compound **R2** does not inhibit neurolysin by a direct effect on the structure of the catalytic machinery.

Binding Occurs Largely through Nonpolar Contacts—The binding of **R2** is dominated by nonpolar and aromatic interactions. Inserted in the hydrophobic pocket, the adamantyl group of the inhibitor contacts the side chains of Ile-123, Met-149, and Leu-155. Steric contacts are also made with other portions of **R2** (Fig. 5, *A* and *B*). Both aromatic rings interact extensively with surfaces of the pocket, and it is clear that these interactions must play an essential role in high affinity binding. Carbons C22-C25 of the C ring, which is buried in the back of the pocket, contact the side chain of Glu-73 from helix 2, and the side chain of Ile-72 interacts with C23 and Cl1 from this ring as well. The F ring stacks face the edge of the phenolic group of another tyrosine, in this case Tyr-76, which also contacts C5 of the pyrazolidine ring. In addition, C13 of F ring contacts Cγ1 of Ile-77, and C16

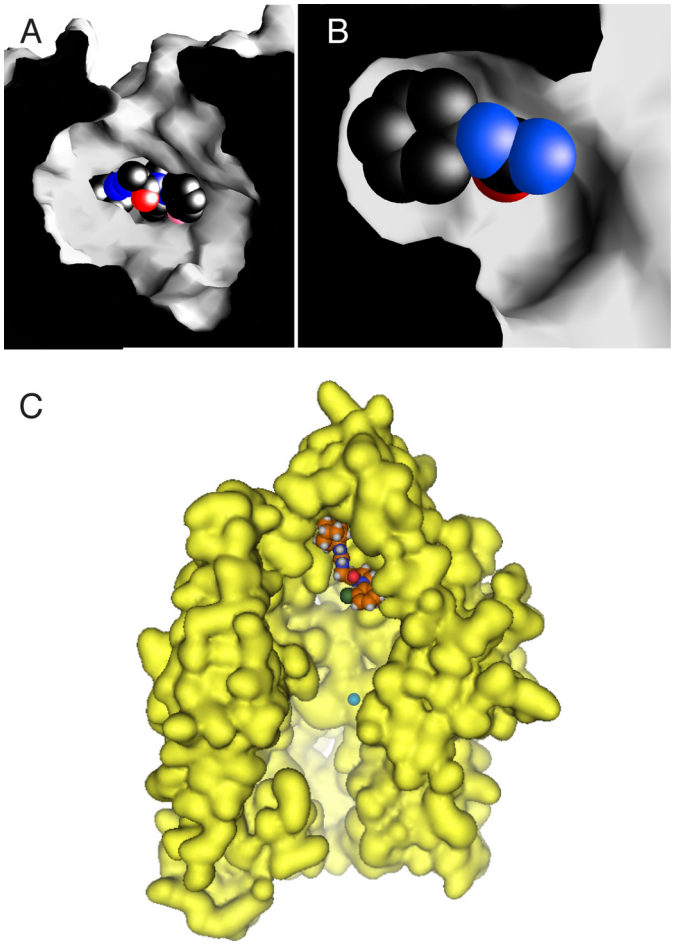

FIGURE 3. *A*, the bound inhibitor. A molecular surface (*gray*) view of the enzyme is shown with the bound **R2** inhibitor in a space filling representation. The view is from the catalytic site of the enzyme along the substrate binding channel. *B*, cut away view of the adamantyl binding pocket. The enzyme is represented as a molecular surface (*gray*) and only the adamantyl and the initial portion of the peptide linker are shown for the inhibitor. *C*, surface view of neurolysin (*yellow*) with computationally docked inhibitor shown in a space filling representation.

interacts with Cγ of Asp-110. Finally the α carbon of Ser-114 packs against the linker at C9.

In contrast to the extensive van der Waals contacts, only one residue makes direct hydrogen bond interactions to the inhibitor. The side chain of Tyr-49 donates a hydrogen bond to one of the carbonyl oxygens (O_2) in the linker region. The side chain hydroxyl of this residue is also positioned 3 Å from the plane of the C ring, in a position to make a O-H/π interaction (59, 60). In addition to these direct interactions, there are two water-mediated contacts between the side chain of Glu-73 and the inhibitor: one to F1 of the F ring and the second, via another water, to O1 of the linker. These water molecules have relatively small refined thermal factors (average B of 15.6 for the four in the two independent neurolysin-**R2** complexes) and are found in both complexes in the crystal asymmetric unit, suggesting that these interactions are stable and may contribute significantly to binding. An additional water molecule accepts a hydrogen bond from N3 of the linker, but this water does not hydrogen bond with any group of the protein either directly or via other ordered solvent molecules. Because the β carbon of the linker alanine does not interact with the enzyme, its influence is likely

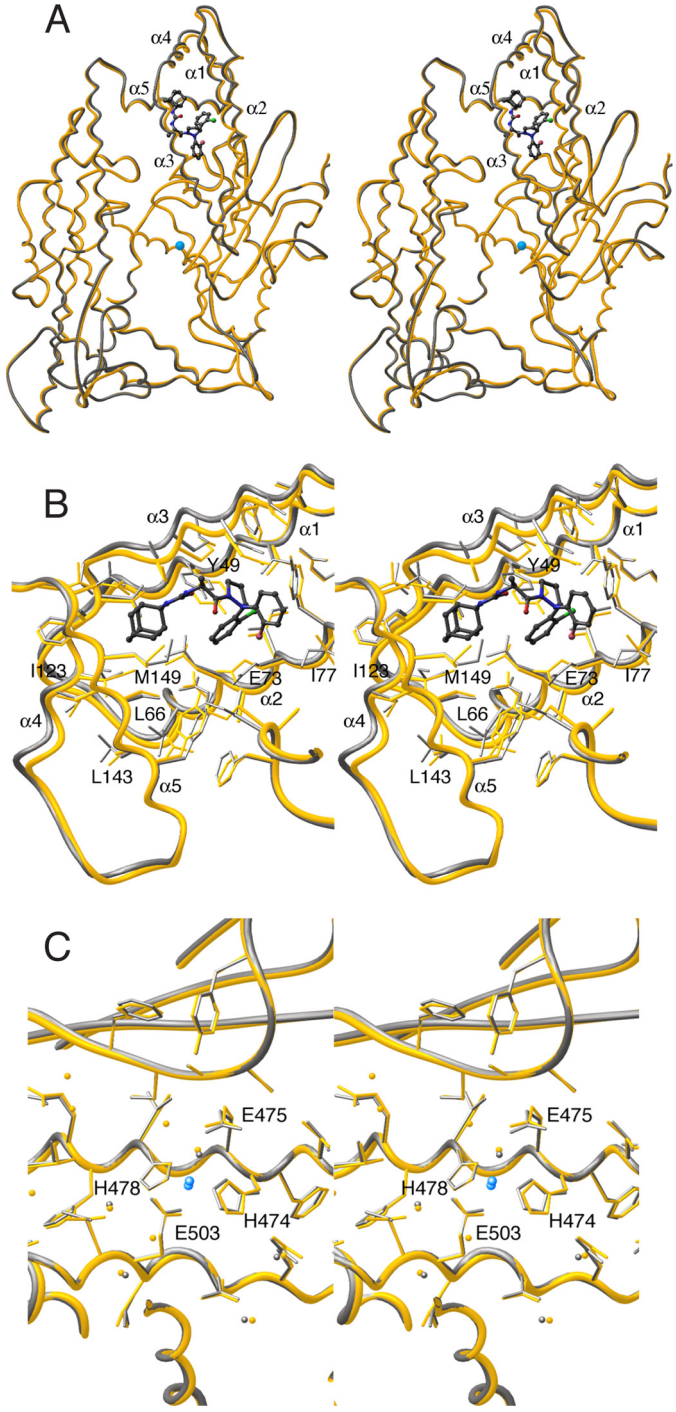

FIGURE 4. **Conformational changes on inhibitor binding.** *A*, overview of backbone changes. *B*, the binding site. *C*, the catalytic site region. In all panels stereo views are shown of the superimposed **R2** complex (*gray*) and the unliganded enzyme (*gold*) (18). Protein backbone is represented by Cα traces, and side chains are shown in stick representations. Inhibitor **R2** is shown also in a stick representation. The exocyclic chlorine and fluorine atoms are shown in *green* and *pink*, respectively, and the catalytic site zinc ion is in *blue*. Key helices and residues are labeled.

an entropic effect, constraining the conformation of the linker in unbound **R2** and decreasing the cost of immobilizing it upon binding. The binding interactions are summarized in Fig. 5*C*.

R2 Is an Allosteric Inhibitor—The observation that **R2** binds away from the catalytic site and does not alter its structure raises the question of how the compound inhibits neurolysin.

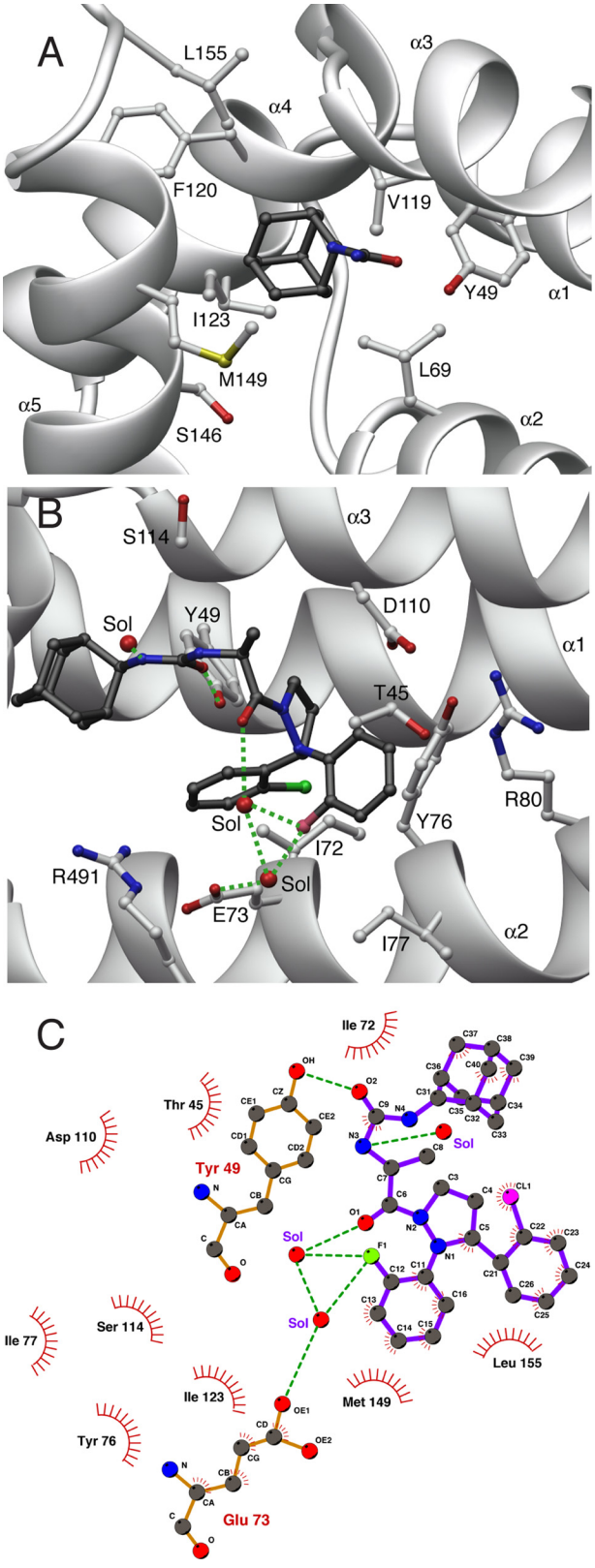

FIGURE 5. **Binding interactions.** Interactions with *A*, the adamantyl group, and *B*, the remainder of inhibitor **R2.** The protein backbone is shown in a ribbons view with key side chains and the inhibitor shown in stick representations. The exocyclic chlorine and fluorine atoms of the inhibitor are shown in *green* and *pink*, respectively. *Dashed green lines* indicate hydrogen bonds. See the text for a description of the interactions. *C*, summary of the binding interactions. Residues in contact with the inhibitor are indicated by the *eyelash-like symbols*, and the *dashed green lines* indicate hydrogen bonds. The two side chains (from Tyr-49 and Glu-73) that make polar interactions with the inhibitor are shown.

TABLE 2
Kinetic inhibition model comparisons for dynorphin A(1–8) and neurotensin hydrolysis

Kinetic model	SS_{rel}[a]	F-test *p* value mixed *vs* other models[b]
Dynorphin A(1–8) substrate		
Competitive	1.052	<0.0001
Noncompetitive	1.011	<0.001
Uncompetitive	3.121	<0.0001
Mixed	1.000	
Neurotensin substrate		
Competitive	2.152	<0.0001
Noncompetitive	3.510	<0.0001
Uncompetitive	5.588	<0.0001
Mixed	1.000	

[a] Relative sum of squares for deviation of a refined model from kinetic progress curve data.
[b] Probability that mixed model does not provide a better fit to the progress curve hydrolysis data than each simpler kinetic model using the Fisher test.

To begin defining this mechanism, we characterized the inhibition kinetics for **R2** with respect to two fluorogenic substrates: dynorphin A(1–8) (Tyr-Gly-Gly-Phe-Leu ⇓ Arg-Arg-Ile) and neurotensin (pGlu-Leu-Tyr-Gln-Asn-Lys-Pro-Arg-Arg-Pro ⇓ Tyr-Ile-Leu). Progress curve data for hydrolysis by neurolysin was fit with competitive, noncompetitive, uncompetitive, and mixed inhibition models and the models were compared using the F-test for nested models. For both substrates, the mixed model with a strong noncompetitive component best represented the data with a high level of significance relative to the other models (Table 2, Fig. 6) and gave low residuals consistent with a good representation of the data (Fig. 7). For the dynorphin A substrate in particular, there was very a little competitive component to inhibition with an α ($= K_i'/K_i$) value, which indicates the degree of competitive inhibition, of 1.1 ($\alpha = 1$ for completely noncompetitive inhibition, and $\alpha > 1$ indicates a competitive component). For the neurotensin substrate, the competitive component is stronger, with an α of 6.1. Nevertheless, it retains a significant noncompetitive component, and the overall kinetic results are consistent with an inhibitor that does not simply sterically exclude substrate from the catalytic site. Kinetic parameters for the mixed inhibition model are given in Table 3. The K_i value for **R2** refines to the low nanomolar range with the data from each substrate.

What then is the mechanism of this mixed inhibition? One possibility for the noncompetitive component is raised by location of the **R2** binding site. As noted, crystal structures of other enzymes with the neurolysin fold demonstrate a clamshell-like conformational change that closes the channel on binding transition state analogs (21, 23). It is likely that a similar motion occurs during the catalytic cycle in neurolysin, and evidence supports this possibility. Soaking crystals of neurolysin and TOP with transition state analogs, for example, disorders or dissolves them consistent with an induced conformational change. Because **R2** binds near the predicted hinge axis for this motion, we considered the possibility that it inhibits neurolysin and TOP by locking the enzyme in the open, inactive conformation.

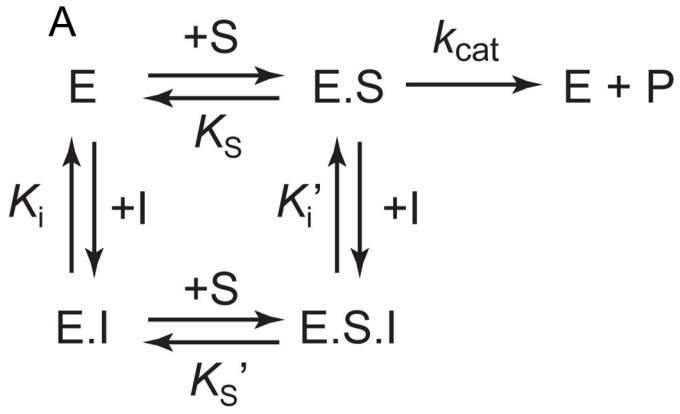

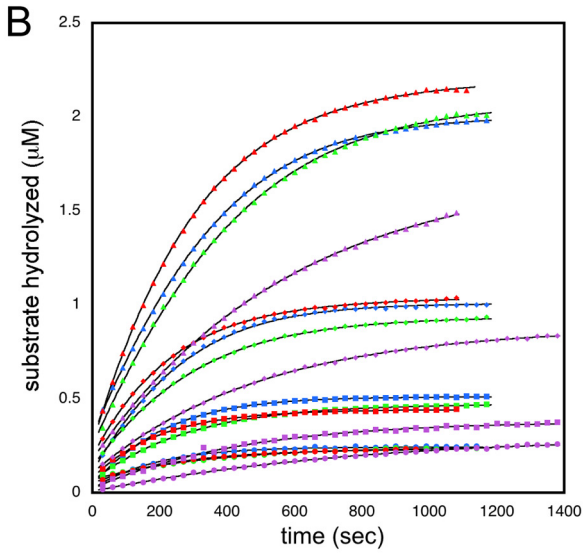

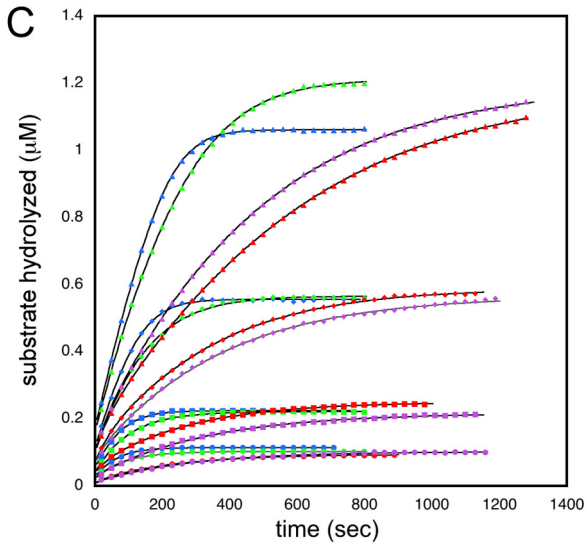

FIGURE 6. **Inhibition kinetics.** *A*, mixed inhibition kinetic model with kinetic parameters and fit of hydrolysis progress curves for *B*, fluorogenic dynorphin A(1–8) and *C*, fluorogenic neurotensin. Model fitting was done with the program DynaFit. Different **R2** inhibitor concentrations are indicated by color (*blue*, no inhibitor; *green*, 0.030 μM; *red*, 0.090 μM; *magenta*, 0.270 μM), and different substrate concentrations are indicated by symbol shape (*circle*, 0.25 or 0.125 μM; *square*, 0.5 or 0.25 μM; *diamond*, 1.0 or 0.5 μM, *triangle*, 2.0 or 1.0 μM; for dynorphin A(1–8) or neurotensin, respectively). Every fifth point from the progress curve data are plotted. Enzyme concentrations were varied as the inhibitor concentration increased, so the curves do not follow a simple pattern of apparent velocities.

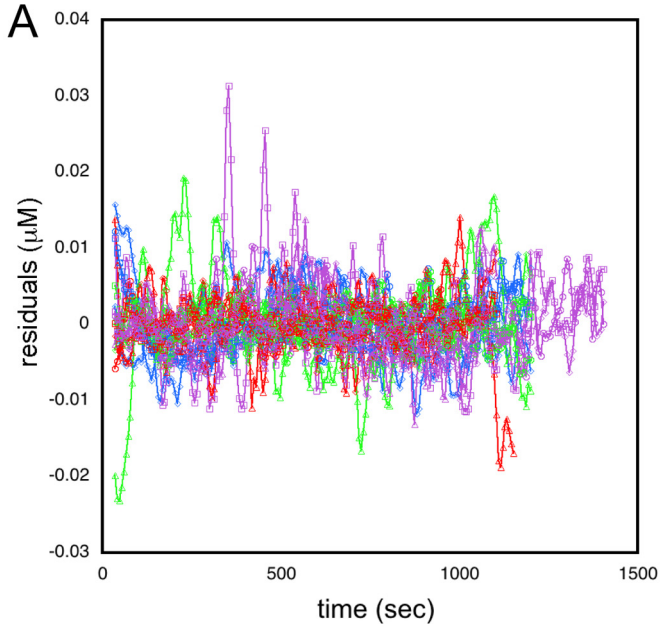

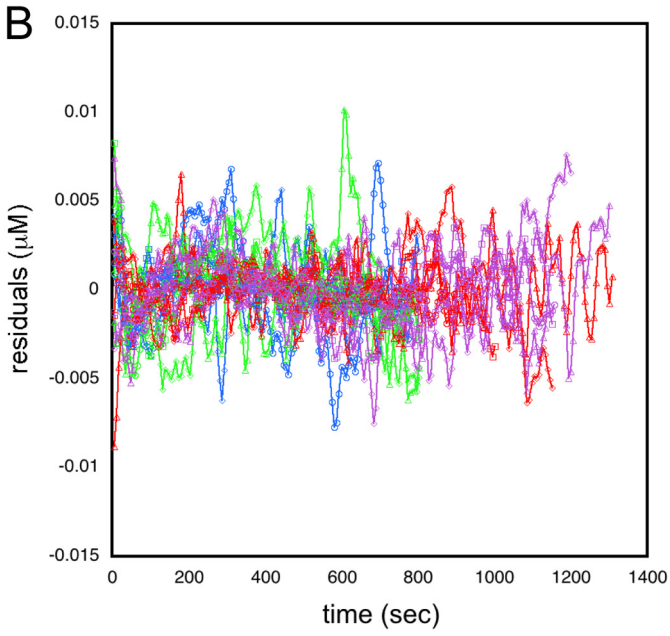

FIGURE 7. **Residuals for fit of the mixed inhibition model.** Residuals from least squares minimized mixed inhibition models for *A*, dynorphin A(1–8), and *B*, neurotensin are plotted. The color and symbol scheme is the same as that used in Fig. 6. For both substrates, the residuals show a random distribution without indication of systematic error in the fit of the model to the data.

The hinge-like motion in the neurolysin-fold enzymes, exemplified by the open and closed forms of ACE2 (23), changes their overall molecular shape enough to alter their hydrodynamic properties. Static fluorescence polarization measurements with pyrene-labeled neurolysin show that adding the inhibitor **R2** to the enzyme produces a significant increase in the measured pyrene emission polarization value over the unliganded enzyme (Fig. 8), consistent with promotion of the open, more slowly rotating, neurolysin conformation. Polarization measurements with a peptide-like, competitive inhibitor phosphodiepril 08 (PPD08) (29, 30) suggest a

TABLE 3
Kinetic parameters for mixed inhibition model

Dynorphin A(1–8) substrate				Neurotensin substrate			
Parameter[a]	Value	Lower bound[b]	Upper bound[b]	Parameter[a]	Value	Lower bound[b]	Upper bound[b]
K_s	0.774 μM	0.766 μM	0.781 μM	K_s	0.180 μM	0.178 μM	0.181 μM
K_s'	0.866 μM	0.856 μM	0.877 μM	K_s'	1.116 μM	1.112 μM	1.119 μM
K_i	0.029 μM	0.027 μM	0.030 μM	K_i	0.018 μM	0.017 μM	0.019 μM
K_i'	0.031 μM	0.029 μM	0.034 μM	K_i'	0.109 μM	0.108 μM	0.110 μM
k_{cat}	0.964 s^{-1}	0.960 s^{-1}	0.968 s^{-1}	k_{cat}	1.502 s^{-1}	1.497 s^{-1}	1.506 s^{-1}
K_m	1.249 μM	1.239 μM	1.258 μM	K_m	0.330 μM	0.328 μM	0.332 μM

[a] See kinetic model (Fig. 6*A*).
[b] Nonsymmetric 95% confidence intervals, lower and upper bounds. See the text under "Experimental Procedures."

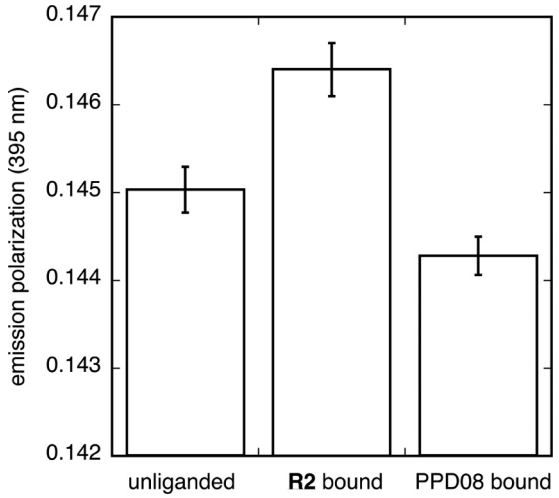

FIGURE 8. **Effects on neurolysin conformation.** Neurolysin tumbling rates were measured by fluorescence polarization as an indication of changes in the conformation of the enzyme upon inhibitor binding. The degree of fluorescence polarization was measured for pyrene-labeled neurolysin alone or neurolysin in the presence of either **R2** or PPD08 inhibitors. Differences in polarization between the unliganded enzyme and **R2** bound enzyme are significant at a 95% confidence level ($p = 0.042$), and differences between R2 bound enzyme and PPD08 bound enzyme are significant at 99% confidence ($p = 0.009$). The difference in measured polarization between the unliganded and PPD08 bound enzyme is not significant at 95% confidence ($p = 0.091$). *Error bars* show mean ± S.E.

decrease in polarization upon binding, consistent with a shift toward the closed conformation, although the difference from the unliganded enzyme is not significant at the 95% confidence level. A shift to the more compact conformation upon binding substrate or substrate-like inhibitor is supported, however, by velocity sedimentation analytical centrifugation where a catalytically compromised neurolysin mutant sediments more rapidly in the presence of saturating amounts of the dynorphin A(1–8) substrate (Fig. 9), suggesting that bound substrate also increases the probability of adopting the closed conformation.

Model calculations indicate that the observed polarization changes observed are consistent with those expected between the open and closed forms of neurolysin. The crystal structure of open neurolysin (18) and a model of the closed form of the enzyme based on the ACE2 structure (23) were used to calculate predicted rotational correlation times under the experimental conditions with HYDROPRO (49). The correlation times were converted to estimated polarization values using the Perrin equation assuming a spherical model. The measured limiting polarization is 0.34, and the effective lifetime of the fluorescent probe as determined from the fluorescence decay curve is 41 ns. The calculated change in polarization at 395 nm is 0.005 for fully open *versus* fully closed conformations, and the observed difference between the **R2** bound (open conformation promoted) and PPD08 (closed conformation promoted) is 0.002. The similar but somewhat smaller experimental values are consistent with the interpretation that the inhibitors promote one or the other conformation but still allow an equilibrium between the two.

These data support an inhibition mechanism where **R2** promotes the open, inactive conformation either in the presence or absence of bound substrate. Consistent with this model, the dynorphin A(1–8) substrate peptide docks in such a way that there is little or no overlap with bound inhibitor reflecting the lack of a strong competitive component of inhibition with this substrate (Fig. 10*A*). The competitive component found for the neurotensin substrate likely arises from a partial overlap of this longer substrate with the **R2** binding site. A peptide with the neurotensin sequence docks into the neurolysin channel with its N-terminal residues extensively occupying the inhibitor binding site (Fig. 10*B*).

DISCUSSION

We have identified and characterized an unusual inhibitor of the metallopeptidase neurolysin that binds remotely from the catalytic site. The interaction pocket for **R2** is sufficiently distant from the catalytic machinery that simple steric exclusion, at least for short peptide substrates, can be ruled out, and inhibition must occur through an allosteric mechanism. Unlike **R2**, nearly all other small molecule inhibitors of metallopeptidases include a functional group that chelates the catalytic site zinc ion (61). The small number of reported nonchelating inhibitors all bind near the catalytic site and act by sterically excluding substrates (62, 63). Inhibitors that bind remotely have advantages over catalytic site-directed compounds in terms of increased specificity and the ability to better tailor the pharmacokinetic properties. The difficulty in developing zinc-chelating inhibitors of matrix metalloproteases that are specific and have desirable drug-like properties (57, 61, 64, 65) illustrates the need for other classes of inhibitors. **R2** represents a promising paradigm for the development of just such a new class of metallopeptidase inhibitors.

The pyrazolidine **R2** has favorable characteristics as a scaffold for the development of therapeutic compounds with enhanced drug-like properties as compared with known inhibitors such as PPD08 (31). In particular, it has only two hydrogen bond donors, an experimentally determined, acceptable logD value of 5.2 at pH 7, and a molecular mass of just over 500 Da. In

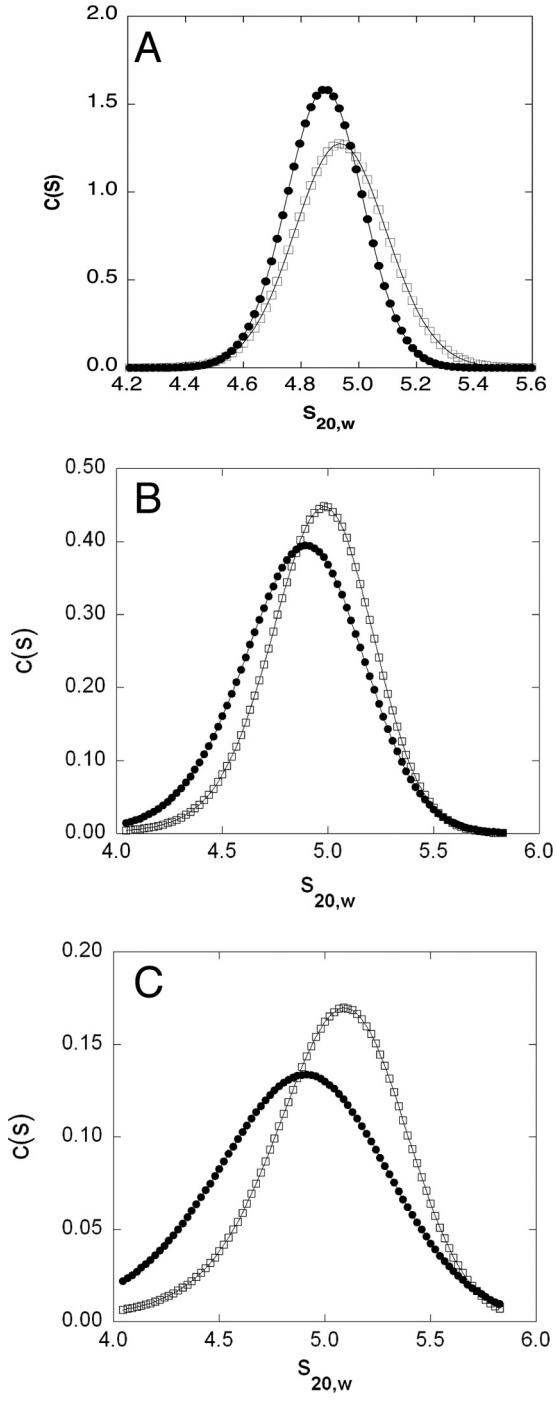

FIGURE 9. **Conformational changes on substrate and inhibitor R2 binding followed by velocity sedimentation ultracentrifugation.** *A*, sedimentation coefficient distributions, *c*(*s*), for 2.2 μM unliganded neurolysin (*filled circles*) and neurolysin in the presence of 110 μM dynorphin A(1–8) peptide (*open squares*). *B*, sedimentation coefficient distributions for 1.1 μM unliganded neurolysin (*filled circles*) and neurolysin in the presence of 110 μM dynorphin A(1–8) peptide (*open squares*). *C*, sedimentation coefficient distributions for 0.55 μM unliganded neurolysin (*filled circles*) and neurolysin in the presence of 110 μM dynorphin A(1–8) peptide (*open squares*). In all cases, the catalytically compromised E475A mutant of neurolysin was used. Sedimentation coefficient distributions have been corrected to values for standard conditions of pure water at 20 °C. *c*(*s*) distributions broaden with decreasing enzyme concentration because the signal-to-noise ratio decreases for the 280-nm absorbance measurements used to follow the protein distribution. Neurolysin sediments more quickly in the presence of saturating amounts of the dynorphin A(1–8) substrate. This result is consistent with bound substrate inducing the closed, more compact, form of the enzyme. The substrate-induced increase in sedimentation coefficient is due to a conformational change rather than partial oligomerization of the enzyme, because the effect is undiminished at lower enzyme concentrations. The average mean value of the sedimentation coefficient distribution for the unliganded enzyme is 4.86 ± 0.01, and the average shift in sedimentation coefficient on substrate binding is 0.11 ± 0.03.

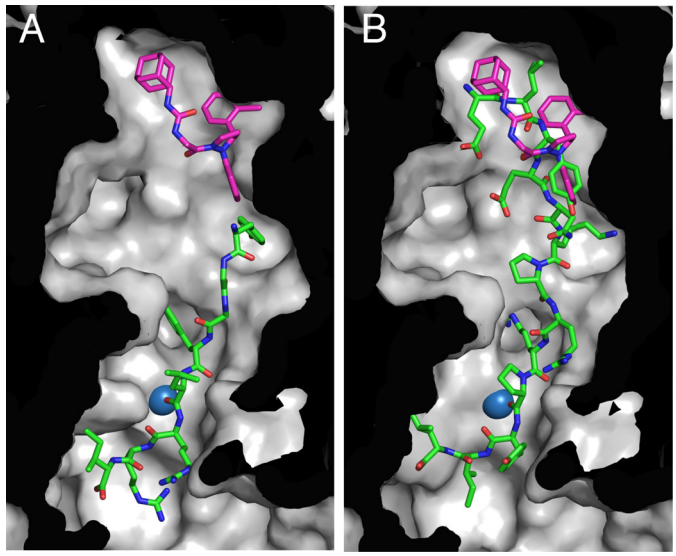

FIGURE 10. **Models of substrate binding in the neurolysin active site channel.** *A*, dynorphin A(1–8) binding model. *B*, neurotensin binding model. Peptides are shown in a stick representation with *green* carbons, and the **R2** inhibitor (placed based on the crystal structure of its complex with neurolysin) is shown with *magenta* carbons. Peptides were docked with the FlexPepDock server in the absence of bound inhibitor, which was then superimposed on the docked structures (see the "Experimental Procedures"). The catalytic site zinc is shown as a *blue sphere*.

addition, its molecular flexibility is low due to a restricted number of rotatable bonds. Finally, it has a favorable calculated polar surface area of 65 Å^2. Compounds having a polar surface area value of 65 Å^2 or less generally display an enhanced ability to cross the blood-brain barrier, whereas compounds above a threshold of 90 Å^2 have been shown to have a low probability of crossing the blood-brain barrier (66).

Allosteric modulation of peptidase activity by both macromolecular and small molecule inhibitors is known. Usually, binding of the modulator is accompanied by a discernable change in the structure of the catalytic site, and the associated functional effects have been attributed to these conformational changes. Examples include binding of a small molecule inhibitor outside the active site of caspase-3, which induces a zymogen-like conformation in active site loops (67), and binding of optimized inhibitory peptides to the exosite of factor VIIa protease, which also alters the conformation of an active site loop (68). In contrast, the inhibitor **R2** has no discernable effect on the structure of the neurolysin catalytic site and causes only modest local changes in the elements surrounding the binding pocket itself. Although subtle structural effects below the level of detection cannot be excluded, it seems likely that some other mechanism accounts for inhibition. Binding of a thrombomodulin fragment to the serine protease thrombin, which enhances proprotein C cleavage by the enzyme, was found to cause little change to the inhibitor-bound catalytic site, suggesting a similarly indirect effect on activity (69). Other studies,

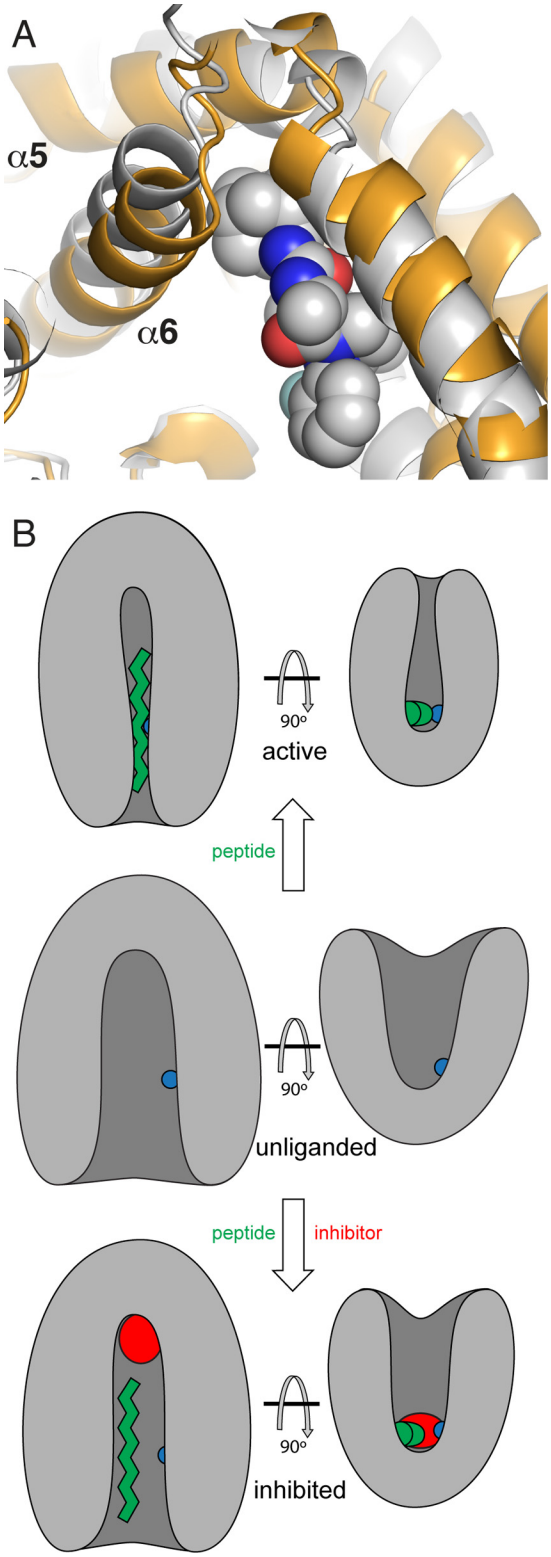

FIGURE 11. **Proposed inhibition mechanism.** *A*, superposition of the neurolysin-**R2** complex (*gray*; **R2** in space-filling representation) with the dipeptidyl carboxypeptidase crystal structure (*gold*) determined by Bode and co-workers (21). The structures were aligned on backbone atoms from residues in the catalytic site region. Intrusion of the closed structure into the **R2** binding site suggests that the inhibitor may sterically restrict the conformational change. *B*, proposed model for neurolysin inhibition by R2. In the center, two schematic views, rotated by 90°, of the unliganded enzyme are shown. The catalytic zinc is drawn as a *blue sphere*. In the upper section, the same two schematic views of the substrate (*green*) bound enzyme are shown, with the hinge like conformational change that is proposed to accompany formation of a catalytically active complex. This hinge motion narrows the active site channel. In the bottom section, the same two views are shown with both bound substrate (*green*) and **R2** inhibitor (*red*). Here the normal hinge-like conformational change is inhibited by the presence of the inhibitor. Longer substrates may compete with the inhibitor for binding.

however, indicate a conformational linkage between the thrombin exocytes and the catalytic center (70, 71), and the underlying mechanism remains obscure.

As noted, we expect a hinge-like motion to accompany substrate binding in neurolysin and TOP, and our kinetic and conformational data suggest that compound **R2** affects enzyme activity by inhibiting this motion. In this model, the noncompetitive component of inhibition results from failure to bring the substrate and catalytic machinery into productive alignment. Initial binding of peptides to the open conformation occurs in a distinct step preceding the conformational change, and for substrates with fewer than 5 or 6 residues N-terminal to the cleavage site, this step would not be affected significantly by inhibitor binding. For longer substrates, such as neurotensin, the inhibitor appears to compete to some extent with substrate binding.

Comparison with the closed form of dipeptidyl carboxypeptidase, which adopts a fold nearly identical to neurolysin (21), suggests a possible mechanism for inhibition of the conformational change by **R2**. Aligning dipeptidyl carboxypeptidase and neurolysin based on the catalytic site region in domain I allows us to assess the changes in the vicinity of the **R2** binding site upon adopting the closed conformation (Fig. 11*A*). In assuming the closed form, domain II pivots about a point at the end of the molecule near the **R2** site. This motion rotates helices 4 and 5, decreasing the size of the **R2** pocket. Thus, the steric incompatibility between the bound **R2** and the closed enzyme conformation could account for the observed inhibition of the enzyme (Fig. 11*B*).

In the open form of ACE2 (23), another member of this fold class, there is also a narrow pocket near the position equivalent to the **R2** binding site in neurolysin. Although the nature and exact placement of this site is different from the **R2** binding pocket, it would still likely be a favorable position for high affinity ligand binding. In the closed form of ACE2 the volume of this site decreases substantially, suggesting that a bound ligand would also inhibit the conformational change in this enzyme. In general, the presence of the neurolysin-fold in a number of other peptidases, including the proven therapeutic target ACE, suggests that inhibiting the hinge motion may be a useful approach for a number of disease states. **R2** may then represent the vanguard of an important new class of therapeutic compounds. These compounds would likely have the advantage of increased specificity over established competitive inhibitors that bind to the catalytic site region. The different competitive inhibitors generally rely on similar binding interactions, including coordinating the zinc ion cofactor, making high levels of specificity difficult to achieve. In contrast, binding sites for compounds that restrict the hinge motion of neurolysin-like peptidases would vary considerably in structure, allowing for enhanced specificity.

Acknowledgments—We thank the staffs of Advanced Photon Source beamline 19-ID (SBC) and beamline 22-ID (SER-CAT) for their help with data collection. Use of the Advanced Photon Source is supported by the United States Department of Energy. We thank Dr. Louis B. Hersh for comments on the manuscript. Use of the Protein Core of the Center for Molecular Medicine was supported by Grant P20 GM103486 from the National Institute of General Medical Sciences.

REFERENCES

1. Rawlings, N. D., Tolle, D. P., and Barrett, A. J. (2004) MEROPS: the peptidase database. *Nucleic Acids Res.* **32,** D160–D164
2. Ketelhuth, D. F., and Bäck, M. (2011) The role of matrix metalloproteinases in atherothrombosis. *Curr. Atheroscler. Rep.* **13,** 162–169
3. Pytliak, M., Vargová, V., and Mechírová, V. (2012) Matrix metalloproteinases and their role in oncogenesis: a review. *Onkologie* **35,** 49–53
4. Meier, P., Maillard, M., and Burnier, M. (2005) The future of angiotensin II inhibition in cardiovascular medicine. *Curr. Drug Targets Cardiovasc. Haematol. Disord.* **5,** 15–30
5. Konkoy, C. S., and Davis, T. P. (1996) Ectoenzymes as sites of peptide regulation. *Trends Pharmacol. Sci.* **17,** 288–294
6. Barrett, A. J., Brown, M. A., Dando, P. M., Knight, C. G., McKie, N., Rawlings, N. D., and Serizawa, A. (1995) Thimet oligopeptidase and oligopeptidase M or neurolysin. *Methods Enzymol.* **248,** 529–556
7. Oliveira, V., Campos, M., Hemerly, J. P., Ferro, E. S., Camargo, A. C., Juliano, M. A., and Juliano, L. (2001) Selective neurotensin-derived internally quenched fluorogenic substrates for neurolysin (EC 3.4.24.16): comparison with thimet oligopeptidase (EC 3.4.24.15) and neprilysin (EC 3.4.24.11). *Anal. Biochem.* **292,** 257–265
8. Rioli, V., Kato, A., Portaro, F. C., Cury, G. K., te Kaat, K., Vincent, B., Checler, F., Camargo, A. C., Glucksman, M. J., Roberts, J. L., Hirose, S., and Ferro, E. S. (1998) Neuropeptide specificity and inhibition of recombinant isoforms of the endopeptidase 3.4.24.16 family: comparison with the related recombinant endopeptidase 3.4.24.15. *Biochem. Biophys. Res. Commun.* **250,** 5–11
9. Alexacos, N., Pang, X., Boucher, W., Cochrane, D. E., Sant, G. R., and Theoharides, T. C. (1999) Neurotensin mediates rat bladder mast cell degranulation triggered by acute psychological stress. *Urology* **53,** 1035–1040
10. Rostène, W., Brouard, A., Dana, C., Masuo, Y., Agid, F., Vial, M., Lhiaubet, A. M., and Pelaprat, D. (1992) Interaction between neurotensin and dopamine in the brain: morphofunctional and clinical evidence. *Ann. N.Y. Acad. Sci.* **668,** 217–231
11. Margeta-Mitrovic, M., Grigg, J. J., Koyano, K., Nakajima, Y., and Nakajima, S. (1997) Neurotensin and substance P inhibit low- and high-voltage-activated Ca^{2+} channels in cultured newborn rat nucleus basalis neurons. *J. Neurophysiol.* **78,** 1341–1352
12. Sharma, R. P., Janicak, P. G., Bissette, G., and Nemeroff, C. B. (1997) CSF neurotensin concentrations and antipsychotic treatment in schizophrenia and schizoaffective disorder. *Am. J. Psychiatry* **154,** 1019–1021
13. Kinkead, B., and Nemeroff, C. B. (2004) Neurotensin, schizophrenia, and antipsychotic drug action. *Int. Rev. Neurobiol.* **59,** 327–349
14. Ertl, G., Bauer, B., Becker, H. H., and Rose, G. (1993) Effects of neurotensin and neuropeptide Y on coronary circulation and myocardial function in dogs. *Am. J. Physiol.* **264,** H1062–H1068
15. Pang, X., Alexacos, N., Letourneau, R., Seretakis, D., Gao, W., Boucher, W., Cochrane, D. E., and Theoharides, T. C. (1998) A neurotensin receptor antagonist inhibits acute immobilization stress-induced cardiac mast cell degranulation, a corticotropin-releasing hormone-dependent process. *J. Pharmacol. Exp. Ther.* **287,** 307–314
16. Fredrickson, P., Boules, M., Lin, S. C., and Richelson, E. (2005) Neurobiologic basis of nicotine addiction and psychostimulant abuse: a role for neurotensin? *Psychiatr. Clin. North Am.* **28,** 737–751
17. Luttinger, D., Nemeroff, C. B., and Prange, A. J. (1982) The effects of neuropeptides on discrete-trial conditioned avoidance responding. *Brain Res.* **237,** 183–192
18. Brown, C. K., Madauss, K., Lian, W., Beck, M. R., Tolbert, W. D., and Rodgers, D. W. (2001) Structure of neurolysin reveals a deep channel that limits substrate access. *Proc. Natl. Acad. Sci. U.S.A.* **98,** 3127–3132
19. Matthews, B. W., Weaver, L. H., and Kester, W. R. (1974) The conformation of thermolysin. *J. Biol. Chem.* **249,** 8030–8044
20. Ray, K., Hines, C. S., Coll-Rodriguez, J., and Rodgers, D. W. (2004) Crystal structure of human thimet oligopeptidase provides insight into substrate recognition, regulation, and localization. *J. Biol. Chem.* **279,** 20480–20489
21. Comellas-Bigler, M., Lang, R., Bode, W., and Maskos, K. (2005) Crystal structure of the *E. coli* dipeptidyl carboxypeptidase Dcp: further indication of a ligand-dependent hinge movement mechanism. *J. Mol. Biol.* **349,** 99–112
22. Natesh, R., Schwager, S. L., Sturrock, E. D., and Acharya, K. R. (2003) Crystal structure of the human angiotensin-converting enzyme-lisinopril complex. *Nature* **421,** 551–554
23. Towler, P., Staker, B., Prasad, S. G., Menon, S., Tang, J., Parsons, T., Ryan, D., Fisher, M., Williams, D., Dales, N. A., Patane, M. A., and Pantoliano, M. W. (2004) ACE2 x-ray structures reveal a large hinge-bending motion important for inhibitor binding and catalysis. *J. Biol. Chem.* **279,** 17996–18007
24. Arndt, J. W., Hao, B., Ramakrishnan, V., Cheng, T., Chan, S. I., and Chan, M. K. (2002) Crystal structure of a novel carboxypeptidase from the hyperthermophilic archaeon *Pyrococcus furiosus*. *Structure* **10,** 215–224
25. Natesh, R., Schwager, S. L., Evans, H. R., Sturrock, E. D., and Acharya, K. R. (2004) Structural details on the binding of antihypertensive drugs captopril and enalaprilat to human testicular angiotensin I-converting enzyme. *Biochemistry* **43,** 8718–8724
26. Holland, D. R., Tronrud, D. E., Pley, H. W., Flaherty, K. M., Stark, W., Jansonius, J. N., McKay, D. B., and Matthews, B. W. (1992) Structural comparison suggests that thermolysin and related neutral proteases undergo hinge-bending motion during catalysis. *Biochemistry* **31,** 11310–11316
27. Grams, F., Dive, V., Yiotakis, A., Yiallouros, I., Vassiliou, S., Zwilling, R., Bode, W., and Stöcker, W. (1996) Structure of astacin with a transition-state analog inhibitor. *Nat. Struct. Biol.* **3,** 671–675
28. Vincent, B., Jiracek, J., Noble, F., Loog, M., Roques, B., Dive, V., Vincent, J.-P., and Checler, F. (1997) Effect of a novel selective and potent phosphinic peptide inhibitor of endopeptidase 3.4.24.16 on neurotensin-induced analgesia and neuronal inactivation. *Br. J. Pharmacol.* **121,** 705–710
29. Jirácek, J., Yiotakis, A., Vincent, B., Checler, F., and Dive, V. (1996) Development of the first potent and selective inhibitor of the zinc endopeptidase neurolysin using a systematic approach based on combinatorial chemistry of phosphinic peptides. *J. Biol. Chem.* **271,** 19606–19611
30. Jirácek, J., Yiotakis, A., Vincent, B., Lecoq, A., Nicolaou, A., Checler, F., and Dive, V. (1995) Development of highly potent and selective phosphinic peptide inhibitors of zinc endopeptidase 24-15 using combinatorial chemistry. *J. Biol. Chem.* **270,** 21701–21706
31. Vincent, B., Dive, V., Yiotakis, A., Smadja, C., Maldonado, R., Vincent, J.-P., and Checler, F. (1995) Phosphorous-containing peptides as mixed inhibitors of endopeptidase 3.4.24.15 and 3.4.24.16: effect on neurotensin degradation *in vitro* and *in vivo*. *Br. J. Pharmacol.* **115,** 1053–1063
32. Lian, W., Chen, G., Wu, D., Brown, C. K., Madauss, K., Hersh, L. B., and Rodgers, D. W. (2000) Crystallization and preliminary analysis of neurolysin. *Acta Crystallograph. D Biol. Crystallogr.* **56,** 1644–1646
33. Otwinowski, Z., and Minor, W. (1997) Processing of x-ray diffraction data collected in oscillation mode. *Methods Enzymol.* **276,** 307–326
34. Brünger, A. T., Adams, P. D., Clore, G. M., DeLano, W. L., Gros, P., Grosse-Kunstleve, R. W., Jiang, J. S., Kuszewski, J., Nilges, M., Pannu, N. S., Read, R. J., Rice, L. M., Simonson, T., and Warren, G. L. (1998) Crystallography & NMR system: a new software suite for macromolecular structure determination. *Acta Crystallogr. D Biol. Crystallogr.* **54,** 905–921
35. Adams, P. D., Afonine, P. V., Bunkóczi, G., Chen, V. B., Davis, I. W., Echols, N., Headd, J. J., Hung, L. W., Kapral, G. J., Grosse-Kunstleve, R. W., McCoy, A. J., Moriarty, N. W., Oeffner, R., Read, R. J., Richardson, D. C., Richardson, J. S., Terwilliger, T. C., and Zwart, P. H. (2010) PHENIX: a comprehensive Python-based system for macromolecular structure solution. *Acta Crystallogr. D Biol. Crystallogr.* **66,** 213–221
36. Kleywegt, G. J., and Jones, T. A. (1998) Databases in protein crystallogra-

phy. *Acta Crystallogr. D Biol. Crystallogr.* **54**, 1119–1131
37. Jones, T. A., Zou, J. Y., Cowan, S. W., and Kjeldgaard, M. (1991) Improved methods for building protein models in electron density maps and the location of errors in these models. *Acta Crystallogr. A* **47**, 110–119
38. Emsley, P., and Cowtan, K. (2004) Coot: model-building tools for molecular graphics. *Acta Crystallogr. D Biol. Crystallogr.* **60,** 2126–2132
39. Carson, M. (1987) Ribbon models of macromolecules. *J. Mol. Graph.* **5,** 103–106
40. Nicholls, A., Sharp, K. A., and Honig, B. (1991) Protein folding and association: insights from the interfacial and thermodynamic properties of hydrocarbons. *Proteins Struct. Funct. Genet.* **11,** 281–296
41. Wallace, A. C., Laskowski, R. A., and Thornton, J. M. (1995) LIGPLOT: A program to generate schematic diagrams of protein-ligand interactions. *Protein Eng.* **8,** 127–134
42. Kuzmic, P. (1996) Program DYNAFIT for the analysis of enzyme kinetic data: application to HIV proteinase. *Anal. Biochem.* **237,** 260–273
43. Kuzmic, P. (2009) DynaFit: a software package for enzymology. *Methods Enzymol.* **467,** 247–280
44. Segel, I. H. (1993) *Enzyme Kinetics: Behavior and Analysis of Rapid Equilibrium and Steady-State Enzyme Systems*, John Wiley & Sons, Inc., New York
45. Reich, J. G. (1992) *Curve Fitting and Modelling for Scientists and Engineers*, McGraw-Hill, New York
46. Bates, D. M., and Watts, D. G. (1988) *Nonlinear Regression Analysis and its Applications*, Wiley, New York
47. Brooks, I., Watts, D. G., Soneson, K. K., and Hensley, P. (1994) Determining confidence intervals for parameters derived from analysis of equilibrium analytical ultracentrifugation data. *Methods Enzymol.* **240,** 459–478
48. Burnham, K. B., and Anderson, D. R. (2002) *Model Selection and Multimodal Inference: a Practical Information-Theoretic Approach*, Springer-Verlag, New York
49. García De La Torre, J., Huertas, M. L., and Carrasco, B. (2000) Calculation of hydrodynamic properties of globular proteins from their atomic-level structure. *Biophys. J.* **78,** 719–730
50. Schuck, P. (2000) Size-distribution analysis of macromolecules by sedimentation velocity ultracentrifugation and lamm equation modeling. *Biophys. J.* **78,** 1606–1619
51. Lamm, T. (1929) Die Differentialgleichung der Ultrazentrifugierung. *Ark. Mat. Astr. Fys.* **21B,** 1–4
52. Laue, T. M., Shah, B. D., Ridgeway, T. M., and Pelletier, S. L. (1992) Computer-aided interpretation of analytical sedimentation data for proteins. in *Analytical Ultracentrifugation in Biochemistry and Polymer Science* (Harding, S. E., Rowe, A. J., and Horton, J. C., eds) pp. 90–125, The Royal Society of Chemistry, Cambridge
53. Cohn, E. J., and Edsall, J. T. (1943) *Proteins, Amino Acids and Peptides as Ions and Dipolar Ions*, Reinhold, New York
54. Raveh, B., London, N., and Schueler-Furman, O. (2010) Sub-angstrom modeling of complexes between flexible peptides and globular proteins. *Proteins Struct. Funct. Genet.* **78,** 2029–2040
55. London, N., Raveh, B., Cohen, E., Fathi, G., and Schueler-Furman, O. (2011) Rosetta FlexPepDock web server: high resolution modeling of peptide-protein interactions. *Nucleic Acids Res.* **39,** W249–W253
56. Feenstra, R. W., Lange, J. H. M., Pras-Raves, M. L., Kruse, C. G., vanStuivenberg, H. H., Tuinstra, T., and Keizer, H. G. (December 2, 2004) Neurotensin: active 2,3-diaryl-pyrazolidine derivatives. U.S. Patent 2004/0242493
57. Cuniasse, P., Devel, L., Makaritis, A., Beau, F., Georgiadis, D., Matziari, M., Yiotakis, A., and Dive, V. (2005) Future challenges facing the development of specific active-site-directed synthetic inhibitors of MMPs. *Biochimie* **87,** 393–402
58. Tyndall, J. D., Nall, T., and Fairlie, D. P. (2005) Proteases universally recognize β strands in their active sites. *Chem. Rev.* **105,** 973–999
59. Malone, J. F., Murray, C. M., Charlton, M. H., Docherty, R., and Lavery, A. J. (1997) X–H$\cdots\pi$(phenyl) interactions: theoretical and crystallographic observations. *J. Chem. Soc. Faraday Trans.* **93,** 3429–3436
60. Steiner, T., and Koellner, G. (2001) Hydrogen bonds with pi-acceptors in proteins: frequencies and role in stabilizing local 3D structures. *J. Mol. Biol.* **305,** 535–557
61. Wasserman, Z. R. (2005) Making a new turn in matrix metalloprotease inhibition. *Chem. Biol.* **12,** 143–144
62. Morales, R., Perrier, S., Florent, J. M., Beltra, J., Dufour, S., De Mendez, I., Manceau, P., Tertre, A., Moreau, F., Compere, D., Dublanchet, A. C., and O'Gara, M. (2004) Crystal structures of novel non-peptidic, non-zinc chelating inhibitors bound to MMP-12. *J. Mol. Biol.* **341,** 1063–1076
63. Chen, J. M., Nelson, F. C., Levin, J. I., Mobilio, D., Moy, F. J., Milakantan, R., Zask, A., and Powers, R. (2000) Structure-based design of a novel, potent, and selective inhibitor for MMP-13 utilizing NMR spectroscopy and computer-aided molecular design. *J. Am. Chem. Soc.* **126,** 9648–9654
64. Brown, S., Meroueh, S. O., Fridman, R., and Mobashery, S. (2004) Quest for selectivity in inhibition of matrix metalloproteinases. *Curr. Top. Med. Chem.* **4,** 1227–1238
65. Skiles, J. W., Gonnella, N. C., and Jeng, A. Y. (2004) The design, structure, and clinical update of small molecular weight matrix metalloproteinase inhibitors. *Curr. Med. Chem.* **11,** 2911–2977
66. Kelder, J., Grootenhuis, P. D., Bayada, D. M., Delbressine, L. P., and Ploemen, J. P. (1999) Polar molecular surface as a dominating determinant for oral absorption and brain penetration of drugs. *Pharm. Res.* **16,** 1514–1519
67. Hardy, J. A., Lam, J., Nguyen, J. T., O'Brien, T., and Wells, J. A. (2004) Discovery of an allosteric site in the caspases. *Proc. Natl. Acad. Sci. U.S.A.* **101,** 12461–12466
68. Dennis, M. S., Eigenbrot, C., Skelton, N. J., Ultsch, M. H., Santell, L., Dwyer, M. A., O'Connell, M. P., and Lazarus, R. A. (2000) Peptide exosite inhibitors of factor VIIa as anticoagulants. *Nature* **404,** 465–470
69. Fuentes-Prior, P., Iwanaga, Y., Huber, R., Pagila, R., Rumennik, G., Seto, M., Morser, J., Light, D. R., and Bode, W. (2000) Structural basis for the anticoagulant activity of the thrombin-thrombomodulin complex. *Nature* **404,** 518–525
70. Verhamme, I. M., Olson, S. T., Tollefsen, D. M., and Bock, P. E. (2002) Binding of exosite ligands to human thrombin. Re-evaluation of allosteric linkage between thrombin exosites I and II. *J. Biol. Chem.* **277,** 6788–6798
71. Croy, C. H., Koeppe, J. R., Bergqvist, S., and Komives, E. A. (2004) Allosteric changes in solvent accessibility observed in thrombin upon active site occupation. *Biochemistry* **43,** 5246–5255